2019

Ice Formation Modes during Flow Freezing in a Small Cylindrical Channel

A. Jain
Purdue University

A. Miglani
Purdue University

Y Huang
Shanghai Jiao Tang University

J. A. Weibel
Purdue University, jaweibel@purdue.edu

S V. Garimella
Purdue University, sureshg@purdue.edu

Follow this and additional works at: https://docs.lib.purdue.edu/coolingpubs

Ice formation modes during flow freezing in a small cylindrical channel

Aakriti Jain[a], Ankur Miglani[a], Yonghua Huang[b], Justin A. Weibel[a] and Suresh V. Garimella[a,*]

[a]*School of Mechanical Engineering, Purdue University, West Lafayette, IN 47907 USA*
[b]*School of Mechanical Engineering, Shanghai Jiao Tong University, Shanghai, 200240 China*

Abstract

Freezing of water flowing through a small channel can be used as a nonintrusive flow control mechanism for microfluidic devices. However, such ice valves have longer response times compared to conventional microvalves. To control and reduce the response time, it is crucial to understand the factors that affect the flow freezing process inside the channel. This study investigates freezing in pressure-driven water flow through a glass channel of 500 μm inner diameter using measurements of external channel wall temperature and flow rate synchronized with high-speed visualization. The effect of flow rate on the freezing process is investigated in terms of the external wall temperature, the growth duration of different ice modes, and the channel closing time. Freezing initiates as a thin layer of ice dendrites that grows along the inner wall and partially blocks the channel, followed by the formation and inward growth of a solid annular ice layer that leads to complete flow blockage and ultimate channel closure. A simplified analytical model is developed to determine the factors that govern the annular ice growth, and hence the channel closing time. For a given channel, the model predicts that the annular ice growth is driven purely by conduction due to the temperature difference between the outer channel wall and the equilibrium ice-water interface. The flow rate affects the initial temperature difference, and thereby has an indirect effect on the annular ice growth. Higher flow rates require a lower wall

---

[*] Corresponding author: sureshg@purdue.edu

temperature to initiate ice nucleation and result in faster annular ice growth (and shorter closing times) than at lower flow rates. This study provides new insights into the freezing process in small channels and identifies the key factors governing the channel closing time at these small length scales commonly encountered in microfluidic ice valve applications.

Keywords

annular ice growth, dendritic ice growth, flow freezing, ice valve, microchannel, supercooled water

Nomenclature

A	channel cross-sectional area	ΔR	change in radius during single time step
c_p	specific heat at constant pressure		
D	channel inner diameter $(D = 2R)$	Re	Reynolds number $(Re = \frac{\dot{m}D}{\mu A})$
h	convective heat transfer coefficient	t	time
k	thermal conductivity	Δt	time step
l	channel length	T	temperature
L	latent heat of fusion	ΔT	temperature difference between ice-
$\dot{m}$	mass flow rate		water interface and the external
n	refractive index		channel wall $(\Delta T = T_i - T_{wall,ext})$
Nu	Nusselt number $(Nu = \frac{hD}{k})$	W	water flow rate $(W = \dot{m}/\rho_l)$
P	pressure	x	transverse position relative to channel
$\dot{Q}$	heat transfer rate		centerline (Fig. 4)
r	radial coordinate	y	vertical position relative to channel
R	channel inner radius		centerline (Fig. 4)

z	axial or streamwise position along the channel centerline (Fig. 4)	ice	ice
		in	inlet
Δz	length of a unit control volume in the axial direction	int	internal
		l	liquid phase (water)

Greek symbols

		lat	latent heat
μ	dynamic viscosity	m	mean
ρ	density	n	nucleation
θ	angle between the normal and incident/refracted light rays	o	initial
		out	outlet

Subscripts

		$open$	open area of channel
ann	annular region	rel	released (energy)
bs	borosilicate glass	s	solid phase (ice)
cav	test cell cavity	$sens$	sensible (energy)
$cond$	conducted heat energy	$wall$	channel wall
$conv$	convected heat energy	$water$	water

Superscript

ext	external		
f	freezing	i	index for a unit control volume
i	ice-water interface	j	index for time step

1. Introduction

Microfluidic systems have been widely employed for chemical and biomedical analysis as they enable high analytical throughput at low sample volumes as well as ease of integration at low cost [1–5]. However, miniaturization and commercialization of fully integrated microfluidic systems

have been hindered by the lack of reliable flow control elements [6]. Flow control is typically achieved through conventional microvalves, which tend to be miniaturized versions of their macroscale counterparts. They are generally actuated through contact between a micromachined orifice and a flexible membrane [7]. Thermal [8,9] or piezoelectric [10,11] actuation deforms the membrane, which makes contact with the valve seat to close the channel. Such microvalves are difficult to fabricate, suffer from unavoidable flow leakage due to the presence of moving elements, and the small gap between the sealing element and the valve seat can generate excessive flow resistance [12].

Considerable effort has been directed at developing innovative microvalves that have alternative actuation mechanisms using phase-change materials including hydrogels [13,14], sol-gels [15], paraffins [16,17], and ice [7,18–22]. This alternative microvalving approach introduces other challenges while benefiting from operation with no moving parts. For instance, all the microvalves, except the hydrogel and the ice-based phase change valves, require an external sensor for timing the valve closure. In hydrogel and paraffin valves, the phase change material is in direct contact with the working fluid, raising contamination and biocompatibility concerns [21]. In addition, accurate positioning of the molten paraffin at the desired location, as required for proper sealing, is difficult [17]. Moreover, once the paraffin solidifies and plugs the channel, an external pressure is required to re-open the valve, thus making it more suitable for a 'one-shot' operation. In contrast, ice valves utilize the working fluid itself as the phase change material to shut off the flow; they are non-invasive and leak-proof, have no moving parts and no dead volume, are free from foreign material, offer no extra flow resistance in the default open state, and are easy to fabricate at low cost. As a result, ice valves have been explored for applications ranging from lab-on-a-chip devices where the rate of reaction can be controlled by freezing the flow of reactants

[7,21] to complex microfluidic systems involving separating and routing fluids [23] by freezing small water droplets that are immiscible with fluids. However, ice valves have a major drawback that they have a long response time on the order of seconds ($\sim$2.5–30 s [18–21]) compared to a few milliseconds (as low as 1 ms [24]) for the conventional microvalves. The long response time is principally due to: (1) the high thermal inertia and limited cooling capacity of the refrigeration systems used to cool the liquid, and (2) the need to supercool the working fluid to temperatures below the freezing point to trigger phase change. To speed up the cooling process, multi-stage thermoelectric cooling units have been employed that generate a large temperature difference between the cooling surface and the channel [22], or the initial temperature of the system has been lowered by pre-cooling the fluid/device. Even with these advances, the response time of current state-of-the-art ice valves remains on the order of 1 s [22].

While most prior studies have focused on design modifications at the device scale or changes in operating conditions, the ice formation and growth process occurring within the channel flow remains relatively unexplored. Once nucleation occurs, water-to-ice conversion takes a finite amount of time [25], which may constitute a considerable duration of the valve response time, depending on the mode of ice formation. The current study focuses on obtaining a more complete understanding of the fundamental flow freezing process occurring inside small cooled channels as a step toward arriving at techniques to reduce the channel closing time.

Several studies [26–38] have explored the different ice formation modes and the thermophysical parameters affecting their growth behavior in supercooled, large-diameter channels under different flow configurations, including stagnant liquid, flow entering an empty channel, and continuous flow through the channel. The temperature history during the freezing of pure water in a cylindrical channel is introduced in Fig. 1 for the canonical case of stagnant

5

conditions [26]. The channel is initially placed into a cold isothermal environment well below the equilibrium freezing point. When the water is cooled, it does not necessarily freeze at the saturation freezing point ($T_f = 0°C$ at atmospheric pressure), but must be cooled by several degrees below T_f before nucleation occurs [27], *i.e.*, the nucleation temperature $T_n < T_f$. For example, the nucleation temperature for normal tap water is 4–6°C below the freezing point [28]. Water existing in liquid phase below the equilibrium freezing point is in a thermodynamically metastable state and is classically termed as undercooled or supercooled water, with the degree of supercooling given by $(T_n - T_f)$. For microchannel closure, the phenomenon of supercooling is important in two ways. First, the time required to achieve supercooling can be long. For example, in a microchannel (233 μm×172 μm×38.2 μm) water had to be supercooled to –17°C before the initiation of nucleation, which required a time of ∼3–8 s [21]. Second, in supercooled water, ice does not grow as a solid layer, but rather as dendrites which can have a markedly faster growth rate and hence affect the channel closing time. As shown in Fig. 1, once nucleation occurs, ice dendrites form within the channel cross-section and a large amount of latent heat is released (at a faster rate than can be removed from the system). This causes the water temperature to increase rapidly to the equilibrium freezing point. Subsequently, the water-to-ice phase change occurs at this constant temperature in the form of a solid ice annulus at the channel circumference, which grows radially inward. Once the channel cross-section is filled, the ice loses sensible heat and its temperature begins to decrease.
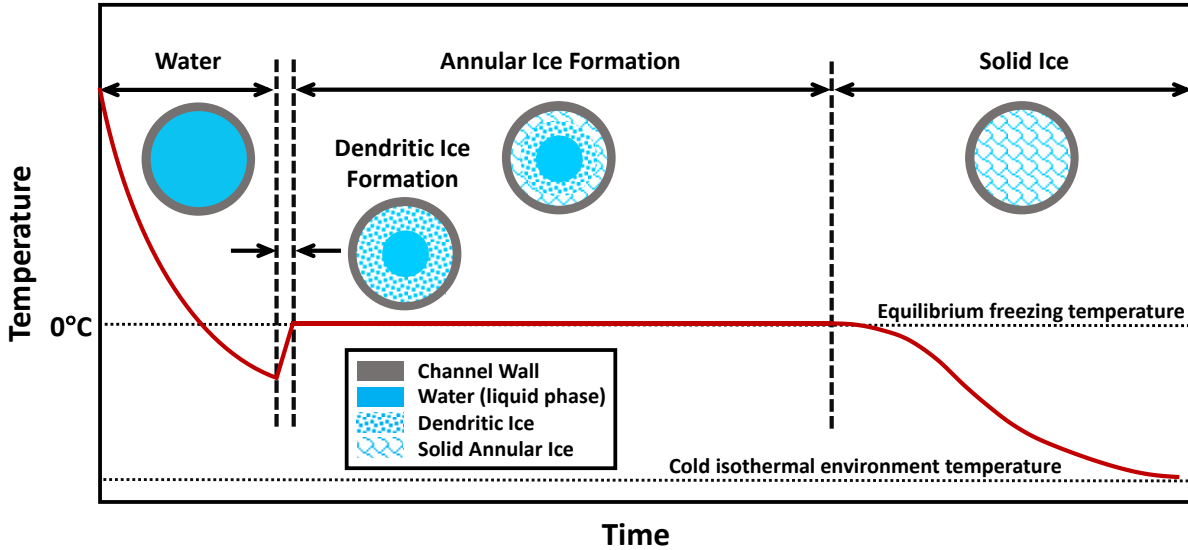
Fig. 1. Schematic representation of the time evolution of water temperature and the corresponding ice formation modes during the freezing of *stagnant* water in a cooled cylindrical channel.

For the case of *stagnant* water, Gilpin [29,30] studied the effect of cooling rate, channel size, and the channel wall material on the growth behavior of dendritic ice in cylindrical channels (copper: $D = 25.4$ mm–99.2 mm and plexiglass: $D = 56.9$ mm–137 mm). The factors that resulted in lower radial thermal gradients and a more uniform temperature profile across the channel cross-section were observed to facilitate dendritic ice formation, *i.e.*, dendritic ice was more likely to form in smaller channel sizes and at slower cooling rates. The channel wall material affected the wall boundary condition (approaching uniform temperature for copper versus uniform flux for plexiglass) and thereby the temperature uniformity in the channel. An expression for the maximum cooling rate required for dendritic ice formation was derived based on the boundary conditions, nucleation temperature, and the channel size. Braga and Milon [34] investigated the effect of the degree of supercooling on the growth behavior of dendritic ice in stagnant water in a channel with internal diameter $D = 45$ mm. The extent of dendritic ice formation was shown to be primarily determined by the temperature distribution existing within the channel at the time of ice nucleation.

When the water was either completely ($-10°C < T_{water} < -5°C$) or partially ($-5°C < T_{water} < 5°C$) supercooled across the cross-section, dendritic ice formed and filled the supercooled portion of the channel. Also, the dendritic ice growth time was shorter as the degree of supercooling was increased. When the water was not supercooled ($T_{water} > 0°C$), no dendritic ice formation was observed. Instead, a solid annulus was formed under these conditions, and took two orders of magnitude greater time to fill the channel (220 s) compared to dendritic ice (6 s).

The freezing of water *entering* an empty pipe was investigated by Gilpin [32], who observed that as water filled an empty supercooled pipe of 10 mm diameter, ice could form and cause pipe blockage through one of the three modes: dendritic, annular, or a dendritic-annular mixed mode. A criterion to determine which mode of formation occurs was proposed based on the wall temperature, the wall material, and the nucleation temperature. Dendritic closure was found to be more probable for pipe wall temperatures close to the freezing point and for lower flow rates, while annular ice appeared at higher wall supercooling and at higher flow rates. Inaba *et al.* [33] extended the work of Ref. [32] to experimentally study the effects of water supercooling temperature on the modes of ice formation during *flow* freezing (*i.e.*, freezing during continuous water flow) in a pipe (D = 15 mm). Again, the dendritic mode was observed at lower degrees of supercooling (*i.e.*, higher absolute temperatures); the radial rate of growth of the dendritic ice front was also significantly higher than that of the annular ice.

Systematic studies on *flow* freezing are limited to channels undergoing flow blockage due to formation of annular ice. In particular, these studies investigated the effect of operating conditions such as the channel wall temperature, liquid supercooling, and the liquid flow rate on the growth rate and heat transfer characteristics of annular ice formation. An early attempt to predict the conditions under which the channel freezes shut was made by DesRuisseaux and Zerkle [35].

Assuming a constant-pressure-driven steady laminar flow in a channel with a parabolic liquid velocity profile and uniform wall temperature, they predicted that the minimum pressure drop needed across the channel to prevent closure for a given liquid increased on decreasing liquid inlet and wall temperatures; their experimental results were in reasonable agreement with the theory. Various studies that have developed analytical models to predict the flow blockage by freezing have found that it depends on the liquid inlet temperature, flow rate, the supercooled channel wall temperature, and the channel size [36–38]; these dependencies have been experimentally verified in Refs. [36,37].

Only a few studies in the literature have modeled flow freezing in *small* channels, each with specific and highly restrictive assumptions. For example, in developing the model for flow freezing, some studies [7, 21] neglected the ice formation completely and assumed that the channel closure occurs instantaneously when water is supercooled to a specified temperature below equilibrium freezing point. A 2-D mathematical model for predicting annular ice growth in square and circular cross-section microchannels was presented by Myers and Low [39]. The channel length was assumed to be much larger than the hydraulic diameter in order to simplify the governing equations based on the lubrication theory. The channel closing time was nearly constant over a large range of flow rates and shown to vary directly with the square of channel diameter and inversely with the temperature difference between the solidification front and the channel wall temperature. While this model fully coupled the flow and freezing processes, it was only valid over a small range of flow rates (0–40 μl/min) and predicted a constant channel closing time over this range of flow rates.

In summary, while flow freezing has been explored in *large* channels and pipes (although closure has often been predicted using highly simplified models), no studies have characterized

the differing ice formation modes that occur during flow freezing in *small* channels suitable for microfluidic ice valve applications, for which the scaling of important transport mechanisms that govern freezing are likely to change with the length scale. Confinement effects that appear on the length scale of intermolecular forces [40-42] are not the focus of this work. High-speed visualization and characterization of the flow freezing phenomenon in such small channels can assist in understanding the factors affecting the modes of ice formation and the flow blockage time.

In a recent study by the authors [43], an experimental facility was developed and demonstrated to control the external cooling boundary conditions during visualization of the ice formation modes in a small channel (500 μm inner diameter). The effect of three constant water flow rates (0.5 ml/min, 1.0 ml/min and 2.0 ml/min) on the growth rate of different ice modes was observed based on the visualizations of the freezing process. In the current study, flow visualizations are synchronized with measurements of the wall temperature and flow rate to analyze the freezing process in a *constant-pressure-driven flow*. Finally, a simplified volume-discretization-based model is developed to determine the factors that influence the annular ice growth. The model uses simple energy balances and a scaling analysis to predict the annular growth duration as a function of flow rate.

2. Experimental Setup and Procedures

2.1 Test facility

The experimental facility consists of a pressure-driven open water flow loop and an open nitrogen (N_2) flow loop that are connected to a test cell (Fig. 2). Water flows through a microchannel in the test cell while the cold N_2 gas flows over the outer channel surface to lower its temperature and initiate freezing of the water; the freezing process is captured by a high-speed

camera. The entire experimental facility (except the cryogenic cylinder) is mounted on a vibration-isolated optical table (VH3648W-OPT, Newport).
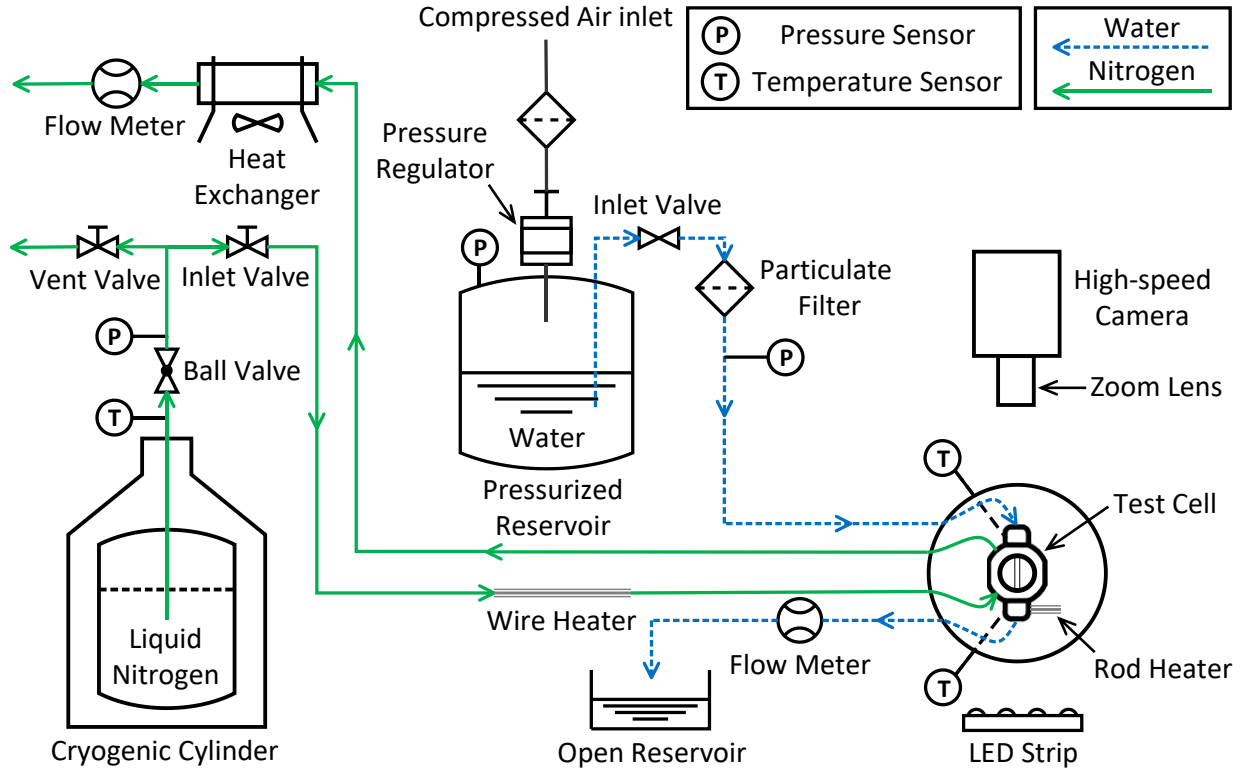

Fig. 2. Schematic diagram of the experimental test facility.

The water flow is driven by the pressure difference between a pressurized reservoir and the ambient. This constant pressure-drop driven open flow loop allows water to enter the channel at precisely controlled, constant flow rates. The reservoir is pressurized with a compressed air source and the desired pressure is maintained using a high-precision servo-controlled pressure regulator (PRG200-25, Omega; ±0.031 kPa). The water pressure, P_{water}, is measured downstream of the reservoir using a pressure transducer (PX302-015GV, Omega; ±0.26 kPa). The water volumetric flow rate is measured using a liquid flow meter (LC-5CCM-D, Alicat; ±0.1 ml/min). The corresponding mass flow rate is determined from the liquid density corresponding to the liquid

temperature recorded at the channel inlet. The water flowing out of the test cell is collected in an open reservoir at ambient pressure.

In the nitrogen open-loop system, a constant-pressure cryogenic cylinder is used to deliver N_2 to the flow loop. To control the cylinder pressure, a pressure relief valve is used to vent N_2 that evaporates continuously inside the cylinder; a pressure gauge measures the cylinder pressure. The nitrogen flow rate is controlled using a ball valve mounted on the cylinder outlet. Downstream of the cylinder, the N_2 flows through an insulated (Cryogel-Z, Aspen) section of pipeline to a T-junction which divides the N_2 flow into two separate flow paths, each with an independently adjustable flow control valve. One path routes to the test cell and is regulated by the N_2 inlet valve; the other path vents to ambient through a vent valve (see Fig. 2). As the nitrogen flows along the line to the test cell, it boils continuously due to the external heating of the line. This generates a large back pressure that can stall the nitrogen flow out of the cylinder. The venting valve is used to vent out some portion of the N_2 to allow for a continuous flow of N_2 out of the cylinder. A T-type thermocouple (TJ36-CPIN-116G-12, Omega; $\pm 1.0°C$) is installed downstream of the cryogenic cylinder and upstream of the T-junction to measure the N_2 temperature.

The temperature of the N_2 gas flowing into the test cell is controlled by a wire heater wrapped around the copper tubing just upstream of the test cell (see Fig. 2). The electrical power to the heater is supplied by an adjustable direct current (DC) power supply (Sorensen, DCS40-25E). The nitrogen leaving the test cell is heated to the ambient temperature using a copper-finned heat exchanger and the flow rate is measured using a 1–5 L/min microturbine gas flow sensor (Cole Parmer, FF-00368-KV; ± 0.2 L/min) before it vents to the ambient.

The test cell (Fig. 3) is a custom component that is 3-D printed using a transparent photo curable material (VeroClear Fullcure810, Objet). The test cell consists of a hollow disk-shaped

cavity (12 mm tall and 25 mm in diameter) with various ports for interfacing with the water flow, nitrogen flow, and measurement probes. The cavity is sealed shut with a 3.6 mm-thick transparent polycarbonate cover to enable visualization. The entire test cell sits inside a circular aluminum enclosure (not shown in Fig. 3), which prevents frost formation on the cell and has glass viewing windows on the top and bottom to permit visualization.
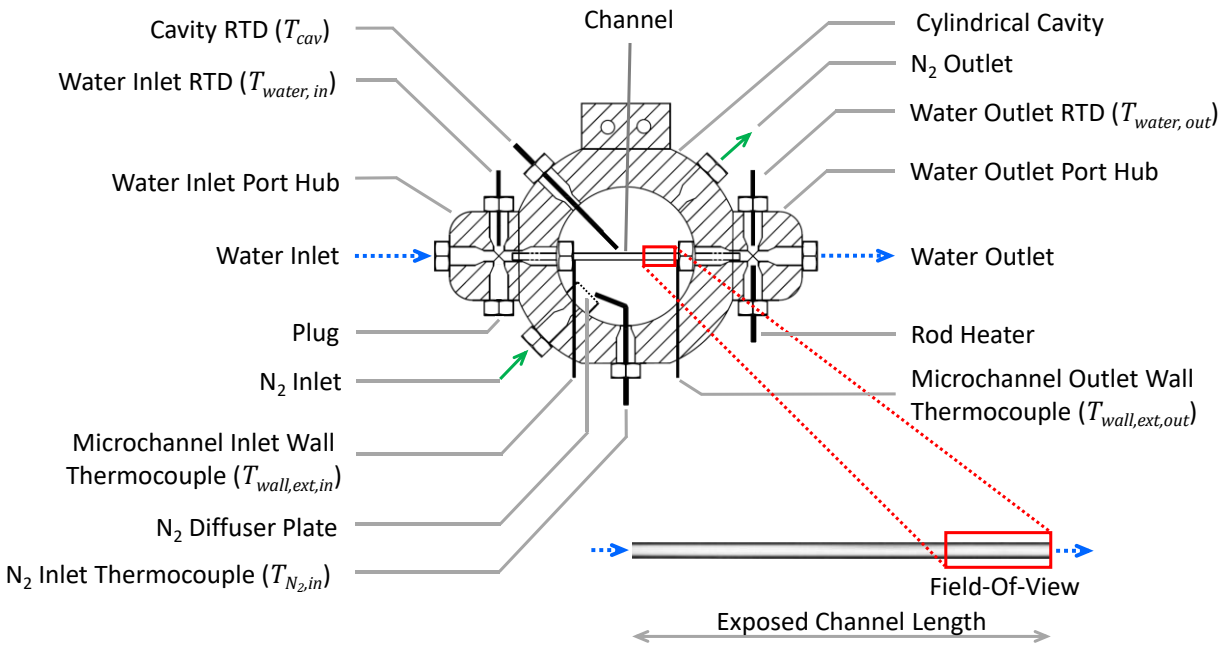

Fig. 3. Sectional view of the test cell (along the horizontal mid-plane) and the measurement instrumentation. Inset shows the exposed channel length and the field-of-view.

A borosilicate glass channel (Vitrocom, CV5070) of circular cross-section with a nominal inner diameter (D) of 500 μm and a wall thickness ($R_{wall,ext} - R_{wall,int}$) of 100 μm is mounted horizontally between two diagonally opposite inner ports in the cavity, as shown in Fig. 3. The non-dimensional channel length exposed to the inside of the cavity l/D is 40. The channel is sealed into the cell at both ends using miniature compression fittings and transparent adhesive silicone epoxy (Momentive, RTV118). The cavity also has two diagonally opposite inlet and

outlet nitrogen ports for flow of the cold nitrogen gas over the channel. A perforated diffuser plate is placed in front of the N_2 inlet port to prevent direct impingement of the incoming cold N_2 gas on to the channel and to achieve uniform temperature surroundings inside the cavity. The nitrogen inlet temperature ($T_{N_2,in}$) is measured using a T-type thermocouple (5TC-TT-T-36-36, Omega; $\pm 1.0°C$) placed in front of the diffuser plate while the cavity temperature (T_{cav}) is measured using a RTD (WZP-100-1/16, Sifang; $\pm 0.1°C$) located close to the cavity center, approximately mid-way along the channel length. Both the thermocouple and the RTD are placed in the same horizontal plane as the channel. The channel external wall temperature is measured using two T-type thermocouples (5TC-TT-T-40-36, Omega; $\pm 1.0°C$) located at each end of the channel. The beads of the wall thermocouple junctions are attached to the channel by carefully placing the bead in contact with the channel wall and wrapping the unsheathed length of the wire (0.6 mm) around the channel. Subsequently, the channel is inspected under a microscope to ensure that there is proper contact between the bead and the wall as well as no other unwanted contacts between the unsheathed wires, except at the junction. Finally, the thermocouples are secured in place by using a thermally conductive epoxy (Duralco 120, Cotronics).

There are two port hubs in the test cell, one at the water inlet side and other on the water outlet side. Each hub contains three ports for the flow paths, water temperature measurements, and rod heater (only used at outlet hub). All the port connections are sealed using miniature compression fittings and epoxy (RTV118, Momentive/GE) to prevent water leakage.

As water flows through the externally cooled channel and its temperature decreases in the streamwise direction, freezing may initiate in the channel after it has entered into the outlet hub region, where the water temperature is lowest and where the freezing process cannot be visualized. To ensure that water is only cooled along the channel length that is exposed to the cavity (*i.e.*, the

visible length), a custom 1/16" (1.59 mm) heater rod, powered using an adjustable DC power supply (XG 100-8.5, Sorenson), was inserted into the outlet hub port. This rod heater warms the outlet hub region, which ensures that the water temperature is lowest in the field-of-view (Fig. 3). It has been experimentally verified that the heating of the outlet hub does not affect the trends in external wall temperature and the channel closing time.

The external wall temperature measurements are recorded at a sampling frequency of 39 Hz using a 20-port data acquisition unit (NetDAQ 2640A, Fluke) with a NetDAQ interface. All other sensor data are recorded at a frequency of 0.22 Hz using another data acquisition unit (34970A, Agilent) with a 20-channel multiplex module using a LabVIEW interface. The power supplied to the heaters is calculated by measuring the voltage drop across them and the current flow across their respective shunt resistors (HA 5 100, Empro).

2.2 Test Procedure

To begin a test, the water line is first completely dried by flushing with dry compressed air for ~30 min. Then the compressed air supply to the reservoir is turned on and the water flow rate is set to 5 ml/min (maximum measurement limit of the flow meter). The reservoir air pressure is then gradually reduced manually using the pressure regulator till the water flow rate decreases to a flow rate that is 0.5 ml/min higher than the desired flow rate.

The cryogenic cylinder pressure is set to a constant value of 77.6 kPa using the pressure control valve mounted on the cylinder. The N_2 flow is then initiated by first opening the N_2 inlet valve completely and then cracking open the vent valve to establish a continuous N_2 supply to the test cell at a constant flow rate of 2.00 L/min. Subsequently, the power to the N_2 heater is turned on and adjusted such that the cavity temperature reaches $T_{cav} = 10°C$ (with a standard deviation of

±2°C over all test runs). The water does not freeze in the channel during the process of setting the cavity temperature due to the elevated initial water flow rate mentioned above. Once the cavity temperature has reached a steady-state condition (standard deviation in T_{cav} over 10 min is less than 1°C), the compressed-air pressure to the reservoir is controlled to reduce the water flow rate to the desired set point. The corresponding constant water pressure (P_{water}) upstream of the test section (downstream of the reservoir) is recorded. It is noted that while the water is driven through the channel by this constant upstream pressure condition throughout the test, the flow rate only remains constant at the set-point until freezing initiates (an increase in the flow resistance of the channel after freezing causes a reduction in the flow rate).

Next, the power to the N₂ gas heater is reduced in a step-wise manner to reduce the cavity temperature and undercool the water until ice is observed to nucleate in the channel. The power steps are chosen such that the cavity temperature reduces by ~4–5°C at each step. At each power level, the system is allowed to attain a steady-state condition where the standard deviations in both T_{cav} and $T_{wall,ext}$ reduce to less than 1°C and the temperature difference between them becomes constant. The outlet hub temperature is kept above freezing by powering the rod heater, for example, to a value of 1.5±0.5 W when T_{cav} reaches to about –8°C.

This test procedure is repeated in a similar manner for multiple trials of each test case. The water flow rates, water pressures, and cavity temperatures at freezing corresponding to the three test cases A, B, and C, averaged over 8 trials for each case, are listed in Table 1.

The temporal variation of external channel wall temperature recorded at the channel inlet and the outlet is highly repeatable, with the inlet temperature data matching the outlet but shifted in time (see Appendix A). This is because the inlet thermocouple has a delayed registration of the temperature jump that occurs after ice nucleation. This delay corresponds approximately to the

time taken by the initial dendritic ice to traverse the entire channel length (from outlet to inlet) following nucleation near the outlet. However, because the thermocouple bead at the outlet obstructs visualization, it was removed for the trials for which synchronous visualization was conducted, and only inlet temperature data are shown.

To ensure that the heating of the outlet hub has no influence on the freezing process, other than shifting the location of nucleation to be within the field of view upstream of the outlet, a separate set of experiments were carried out (keeping the same inlet and boundary conditions) with the rod heater removed. Results from these experiments confirm that the trends in the variation of $T_{wall,ext}$ and the channel closing time remain the same with and without the heater.

Table 1. Test cases and their corresponding water flow rates, upstream water pressure, and the steady state cavity temperatures at freezing. Digits in brackets denote standard deviation in measurements over 8 experimental trials each.

Case	Water flow rate, $W = \dfrac{\dot{m}}{\rho_l}$ (ml/min)	Upstream water pressure, P_{water} (kPa; absolute)	Water inlet temperature, T_{in} (°C)	Cavity temperature, T_{cav} (°C)
A	0.5	9.03	8 (±2)	–27.5 (±9.2)
B	1	22.03	8 (±2)	–33.9 (±4.6)
C	2	39.48	8 (±2)	–56.2 (±5.5)

2.3 Visualization

Ice formation modes during freezing of water flowing through the channel are visualized using a high-speed camera (VEO 710L, Phantom) fitted with a long-working-distance high-

magnification zoom lens (VHZ50L, Keyence). For accurate positioning, the camera and the lens assembly is mounted on a three-axis traversing stage. This assembly was placed vertically above the optical window of the test cell enclosure, with the lens focused on the channel mid-plane in the field-of-view ($0.74 < z/l < 1$), as marked in Fig. 3. The channel is uniformly backlit using an adjustable, high-intensity LED strip with an integrated high efficiency diffuser (BL138, Advanced Illumination).

The images are acquired at a frame rate of 5000 fps with an exposure time of 190 μs using the Phantom PCC software (version v2.8.761.0). An image size of 960×152 pixels is used to visualize the freezing process at a spatial resolution of 6 μm/pixel, which corresponds to an optical magnification of 3.3×. The camera is set in a looping mode to record continuously throughout the test. Once the freezing process is complete, an external end-trigger signal is sent to the camera using a pulse generator (Model 505-4C, Berkeley Nucleonics Corporation), which stops the recording and saves the most recent 17.38 s of recorded frames. The time history of the trigger signal is recorded by a data acquisition unit (NetDAQ 2640A, Fluke) using a NetDAQ interface at a sampling frequency of 39 Hz. This enables synchronization of the temperature and flow rate readings to the high-speed images, so that any change in these readings can be matched to corresponding visualizations of the freezing process inside the channel.

During annular ice growth, the thickness of the solid ice layer is measured using the images as it grows radially inwards from the inside channel wall. However, the actual physical position of the water-ice interface differs from its apparent position in the image due to the optical distortions caused by light refraction at the ice-glass and the glass-gas interfaces. To demonstrate the relationship between actual and apparent location of the annular ice front in the channel, the schematic diagram in Fig. 4(a) shows a quarter-section of the channel cross-section (*x-y* plane)

alongside a sample image of the channel side view (y-z plane) obtained via the experimental visualizations, both aligned along the channel center-line. An accurate measurement of the annular ice thickness is obtained by accounting for these optical distortions in the images, using a refraction correction method reported by Kingston *et al.* [44], as is described in detail in Appendix A.
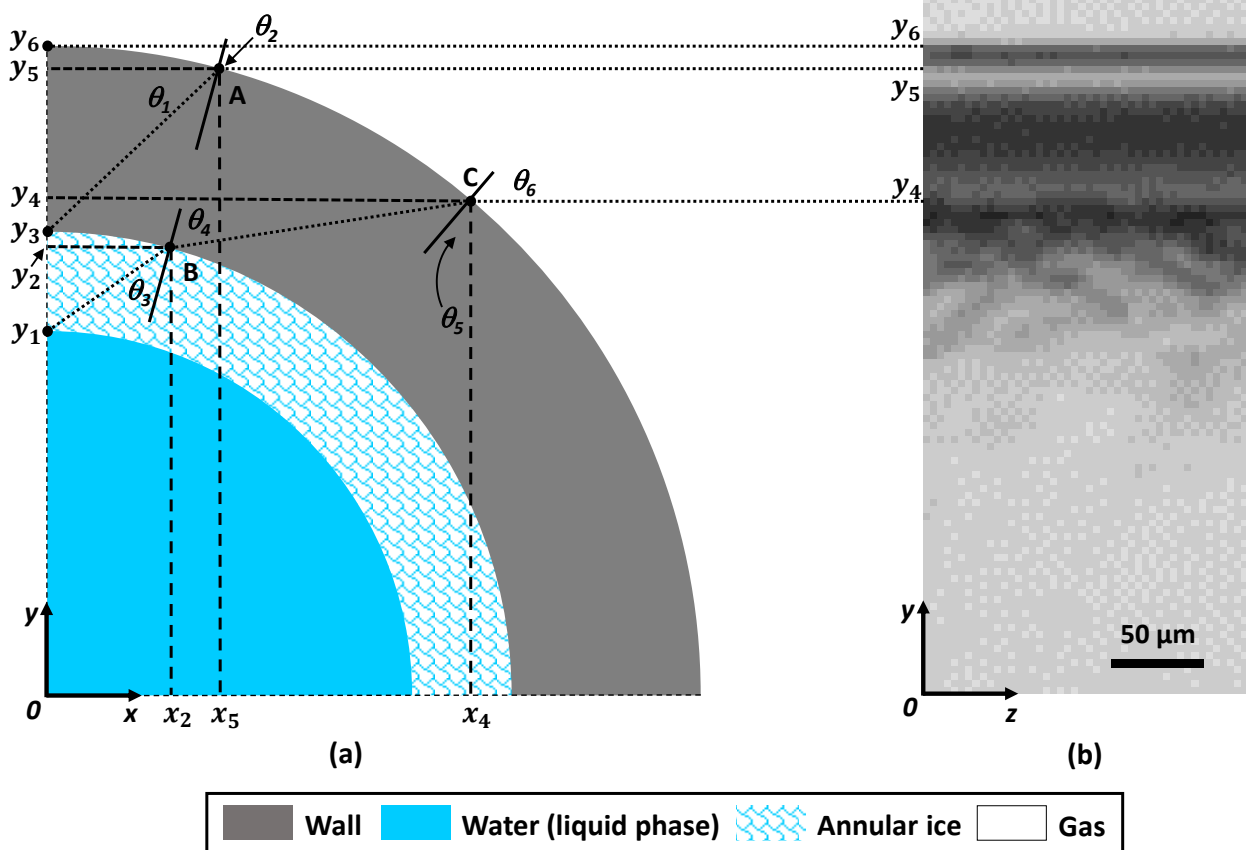

Fig. 4. (a) Schematic diagram illustrating light refraction through ice-glass and glass-gas interfaces and (b) the corresponding high-magnification image captured by the camera. Actual locations of the key points on the interfaces are marked by dots; dotted lines show pathlines traced by light from these points of interest in the x-y plane that are collected by the camera in the y-z plane. Dashed lines mark the x-y position of the points where light is refracted along the pathlines and solid lines indicate the outward normal to the interfaces at the points of refraction.

3. Results and Discussion

The results obtained from flow freezing of water at different flow rates are presented here. As described in Section 2.2, to initiate freezing, the channel external wall temperature is reduced gradually in steps. Freezing initiates suddenly at the water-wall interface at a certain point when the wall temperature is cold enough ($T_{wall,ext}$ = –6.5°C, –9°C and –12.75°C for test cases A, B and C, respectively). During the freezing process, the different modes by which ice forms are identified and their qualitative features are first discussed in Section 3.1 based on the visualization images. These modes are subsequently characterized based on the time history of the external channel wall temperature and the water flow rate, both synchronized with the visualization images. Finally, a simple model is developed to understand the effect of flow rate and channel wall temperature on the annular ice growth responsible for channel closure (Section 3.2).

3.1 Ice Formation Modes

Figs. 5 and 6 show selected images from the high-speed visualizations for test case A during the dendritic and annular modes of ice growth, respectively. These image sequences show the complete process of channel closure starting from dendritic ice nucleation at the channel inside surface to complete flow blockage resulting from inward growth of the annular ice. Similar behavior is observed for cases B and C, as shown with the high-speed videos of all three cases included in Appendix A. Note that air bubbles precipitated from the undegassed water during the freezing process in some tests.

In Fig. 5, dendritic ice nucleation occurs at the water-wall interface near the channel outlet at t = 0.021 s. As water flows through the channel, losing sensible heat along the streamwise direction, it is coldest at the outlet. The position of nucleation is slightly upstream of the outlet by

design (as discussed previously in Section 2.2). Dendritic ice nucleation occurs adjacent to the wall where the water temperature is lowest; the external wall temperature is supercooled as shown by measurements ($T_{wall,ext} = -6.5°C$), and since dendritic ice is formed only in supercooled water [29–34], we infer that the water adjacent to the internal channel wall is also supercooled. Following nucleation, the dendritic ice rapidly grows axially in both upstream and downstream directions from the nucleation point and covers the field of view ($0.74 < z/l < 1$) within $t = 0.21$ s.

Based on the current visualization, inward radial growth of the dendritic ice (*i.e.*, thickness of the dendritic ice layer) cannot be quantitatively characterized from the images. However, it can be inferred from our observations that the dendrites do not fill the entire cross-section. For the dendritic ice to grow radially inward to the center of the channel, the water should be supercooled across the channel cross-section [34]. However, the water temperature measurements at the channel outlet indicate that the bulk temperature is above the equilibrium freezing point ($T_{water,out}$ = 1.2°C), and therefore the water is not supercooled across the entire channel cross-section. In addition, if the dendritic ice filled the entire channel cross-section, it would be expected to cause a significant flow blockage; the flow rate does not reduce suddenly to zero during the period of dendritic ice growth (Fig. 7). Furthermore, it is known from the literature [45–47] that in the presence of a surface, ice dendrites tend to grow along the surface as opposed to into the bulk supercooled water, because the higher thermal diffusivity surface (borosilicate glass in this case, compared to water) acts as a heat sink for the latent heat of fusion released during dendritic ice nucleation and growth.
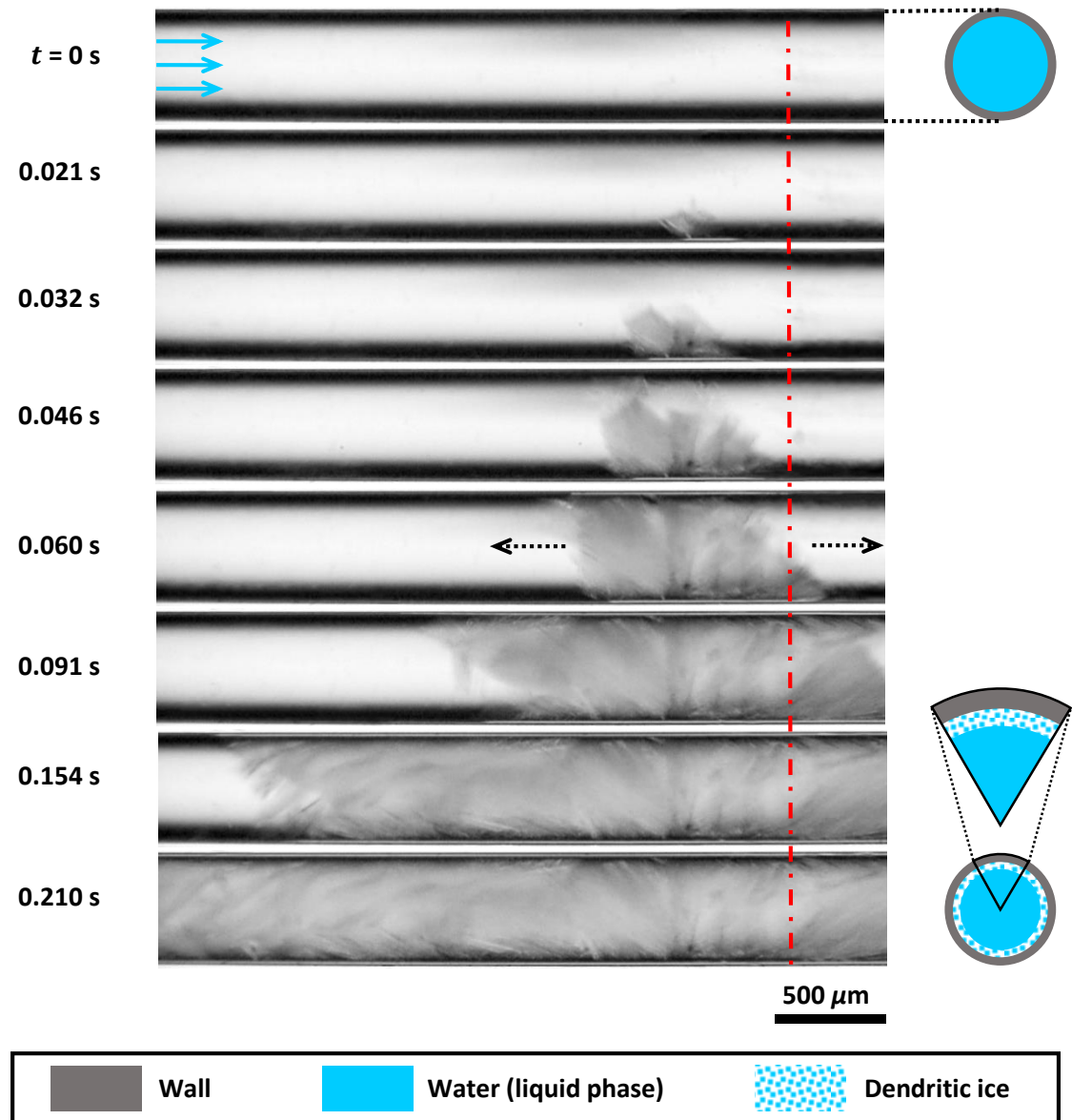
Fig. 5. Time sequence of images showing dendritic ice formation and growth as the freezing initiates in the channel for case A. The schematic diagrams on the right show the channel cross-section at the closure plane (dash-dot red line). The wall, water, and dendritic ice regions are shaded as indicated in the legend. Flow direction is from left to right.

The formation of dendritic ice is accompanied by a large latent heat release which leads to a rapid increase in the channel wall temperature and brings the ice-water interface temperature to

the equilibrium freezing point ($T_i = 0°C$). This is evident from Fig. 7 which shows the time history of the external channel wall temperature and flow rate measured during the period of freezing and channel closure. Starting from an initial steady state ($T_{wall,ext} = -6.5°C$), there is a sharp jump in the external wall temperature shortly following the dendritic ice nucleation. The short delay between nucleation and the temperature rise is due to the finite amount of time taken for the dendritic ice to traverse the channel length and reach the inlet where the temperature is measured (see Appendix A). Subsequently, $T_{wall,ext}$ continues to rise as the water adjacent to the channel inside surface converts to dendritic ice with a simultaneous release of latent heat of fusion, until at $t \approx 1$ s when the dendritic ice front has covered the entire channel length ($0 < z/l < 1$). After this time, $T_{wall,ext}$ stabilizes at a constant value of $-2°C$. This dendritic ice growth period is indicated in the bar at the top in Fig. 7. Note that the image sequence shown in Fig. 5 corresponds to the initial 0.21 s of this period, during which only one-fourth of the channel length near the outlet ($0.74 < z/l < 1$) is covered by dendritic ice. As shown in Fig. 6, a short time after dendritic ice covers the entire channel length, a thin layer of solid annular ice starts to appear at the channel circumference at $t = 1.06$ s, close to the channel outlet. This solid ice annulus grows radially inwards until it fills the channel cross-section at the closure plane at time $t = 3.75$ s.
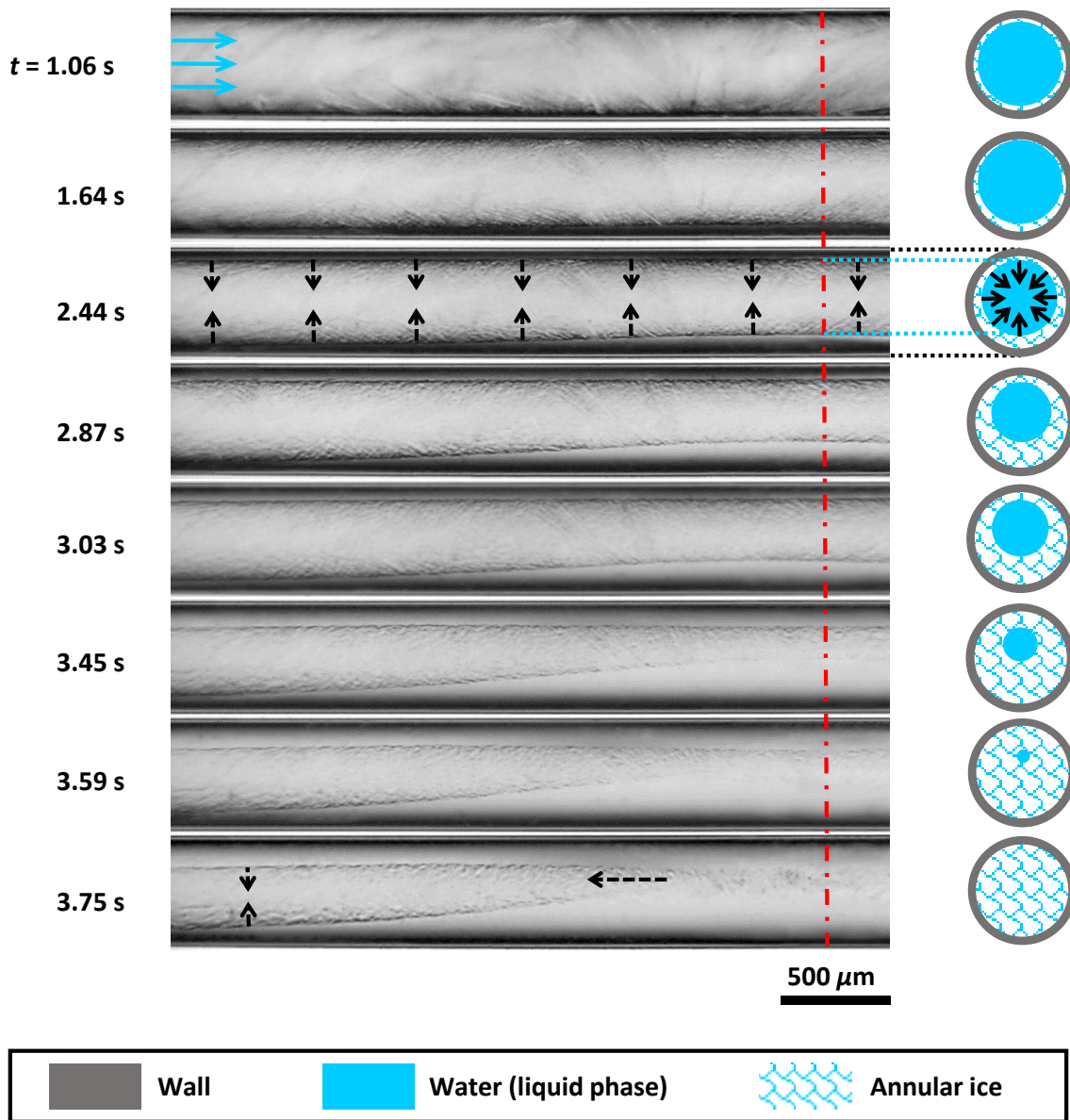
Fig. 6. Time sequence of images showing annular ice growth and closure in the channel for case A. The schematic diagrams on the right show the channel cross-sections at the closure plane (dash-dot red line) with the wall, water, and ice regions shaded as indicated in the legend. Flow direction is from left to right. The black dashed arrows indicate the direction of annular ice growth.

Fig. 7 shows that the external wall temperature is nearly constant at –2°C (with a standard deviation of ±0.5°C over all experimental runs) during the period of annular ice growth. It is

reasonable to assume that the ice-water interface temperature remains constant at the equilibrium freezing temperature of $T_i = T_f = 0°C$ during the annular ice growth phase, such that the temperature difference between the external channel wall and ice-water interface is constant at $(T_i - T_{wall,ext}) = 2\pm0.5°C$. As the annular ice grows and becomes substantially thick such that the channel is nearing closure (at ~3.45 s in Figs. 6 and 7), the ice begins to lose sensible heat and the external wall temperature starts to drop.
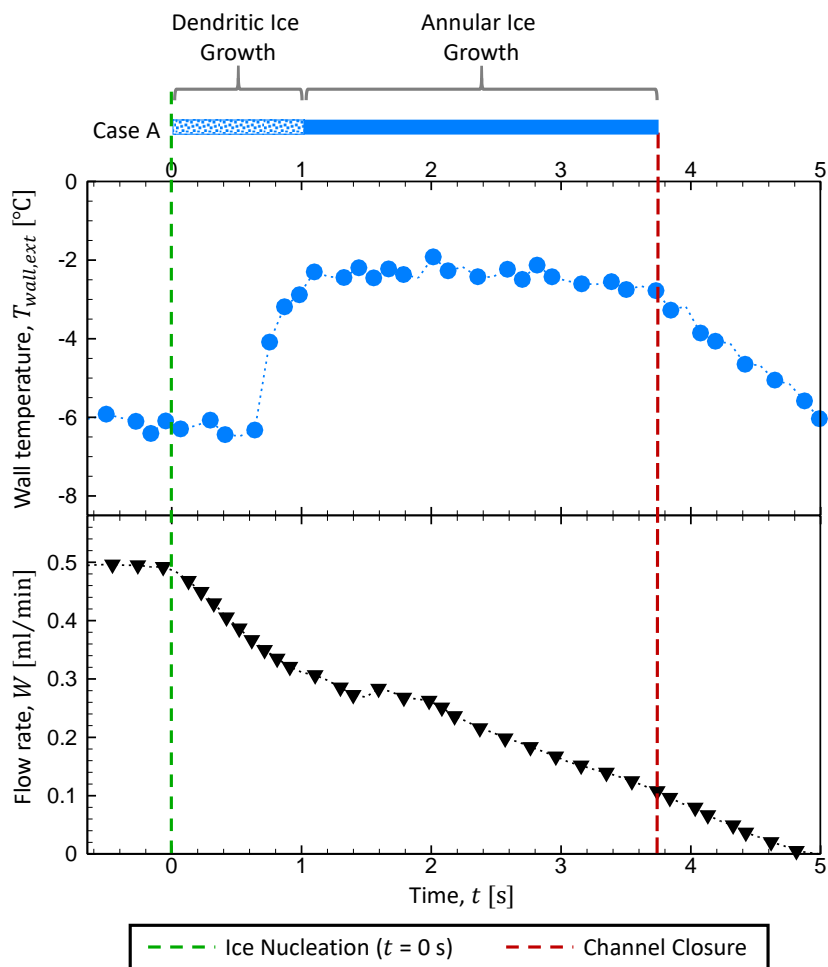

Fig. 7. Synchronized temporal variations of the wall temperature and the water flow rate as freezing occurs for test case A. The durations of dendritic and annular ice growth are indicated in the bar on the top. The water inlet temperature is maintained constant at 8 ($\pm$2)°C.

It is evident from Fig. 7 that there is a noticeable drop in the flow rate during dendritic ice growth, but it is still far above zero. In contrast, as the solid annulus grows and narrows the flow cross-section, there is a continuous reduction in the flow rate, which ultimately drops to zero when annular ice fills the channel at the closure plane. Thus, under the present test conditions, dendritic ice only partially blocks the flow (as it grows along channel surface) while radial inward growth of annular ice leads to the complete flow blockage. In this study, channel closing time is defined as the total duration from nucleation to closure of the annulus, which includes the periods of both dendritic and annular ice growth. Channel closing time is measured as the time between the frame when dendritic ice is first observed (Fig. 5) and the frame where the top and bottom annular ice fronts merge (Fig. 6). For case A, the total channel closing time is 3.75 s, out of which the duration of dendritic ice growth (~1 s) is smaller compared to the duration of annular ice growth (~2.7 s).

Fig. 8 shows a comparison of the time history of external channel wall temperature $T_{wall,ext}$ during freezing for test cases A, B, and C. The data from each different case are aligned in time such that $t = 0$ s corresponds to the instant of ice nucleation. In Fig. 8, firstly, the external wall temperature at the time of ice nucleation decreases with an increase in flow rate, which indicates that water is supercooled to lower temperatures at higher flow rates before the nucleation begins. This is also indicated by the shorter period of dendritic growth at the highest flow rate (0.6 s for case C compared to 0.7 s and 1.1 s for cases B and A, respectively), because dendritic ice grows faster with an increase in the degree of supercooling [34]. Secondly, the annular ice growth duration decreases monotonically from case A to C (2.7 s, 1.9 s, and 0.8 s for cases A, B and C, respectively). Finally, the constant $T_{wall,ext}$ during annular ice growth decreases (*i.e.*, ΔT increases) with an increase in flow rate ($T_{wall,ext} = -2°C$, $-3.5°C$ and $-7°C$ for cases A, B and C, respectively).
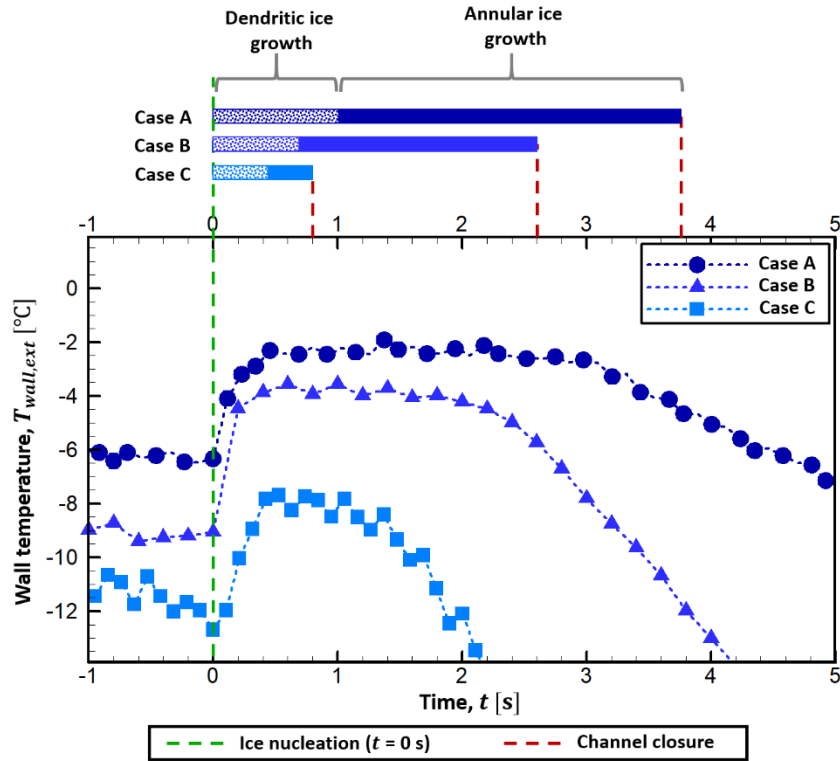
Fig. 8. A comparison of temporal variation of the wall temperature for the three test cases. The bar on top shows a comparison of the periods of dendritic and annular ice growth.

A comparison between the growth behaviors of the two ice formation modes shows that annular ice growth dictates the channel closure. Based on this observation, the next section presents a simplified model that provides an understanding of how the operating parameters influence the annular ice growth time.

3.2 Model Description

A simplified volume-discretization based model is developed to predict the growth of annular ice thickness during the transient freezing of water flowing inside a straight, cylindrical channel using a lumped system analysis. The following assumptions and simplifications are used in the model formulation:

1. The flow is axisymmetric, laminar, and incompressible.

2. The fluid has a well-defined, distinct freezing point and the phase properties are temperature-independent.

3. The discretized elements are assumed to be lumped masses for heat transfer analysis, *i.e.*, the flow has a uniform velocity $\left(V = \dot{m}/\rho_l A\right)$ and temperature profile across the channel cross-section.

4. There is no conduction in the axial direction.

5. The annular ice layer is flat and parallel to the channel wall at each streamwise location.

The model considers annular ice growth from an initial condition at which a thin solid annular ice layer of initial thickness $(R_{wall,int} - R_0)$ is already developed at $t = 0$ s. This is to allow direct comparison to the experiments during which the thin layer of annular ice can only be observed above some minimum thickness. Also, as discussed previously in Section 3.1, the annular ice is observed to grow under an isothermal wall condition; hence, the external wall temperature is taken as a constant boundary condition that is lower than the equilibrium freezing point of water.

3.2.1 Modeling approach

As shown in Fig. 9, a channel with external and internal radii of $R_{wall,ext}$ and $R_{wall,int}$, respectively, is uniformly discretized into small control volumes (CV) of length Δz in the axial direction, each encompassing the entire channel cross-section. The channel external wall temperature, $T_{wall,ext}$, is maintained at a uniform value lower than the freezing temperature, T_f, along the entire length. The water enters the channel at a constant inlet mass flow rate of $\dot{m}_0$ and a mean inlet temperature of T_0 $(> T_f)$. Time is discretized in steps of Δt.
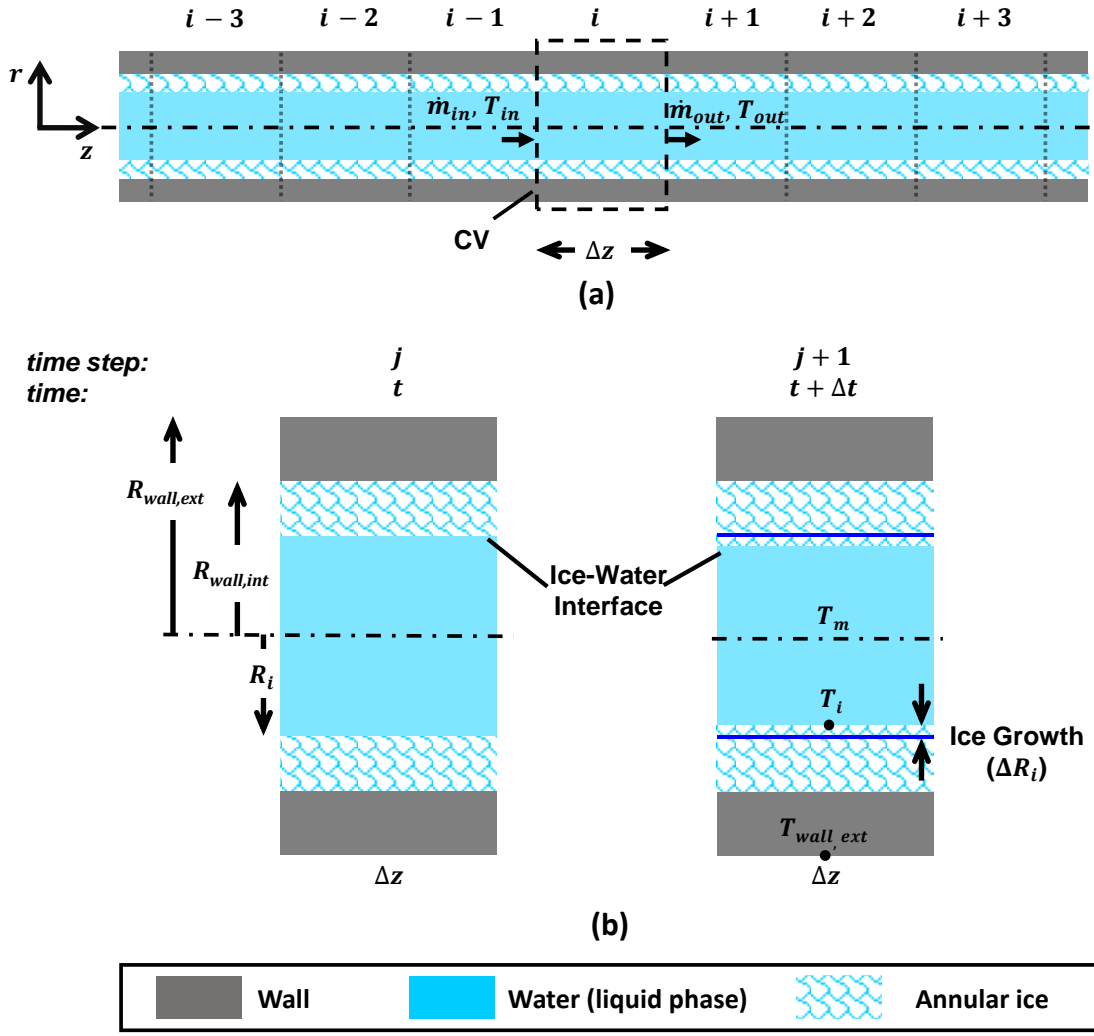
Fig. 9. Schematic diagrams illustrating (a) the control volumes in the channel and (b) the ith control volume at times t and $t + \Delta t$.

Fig. 9(b) illustrates a zoomed-in view of a single control volume i at time step j. An annular ice layer with interface radius $R_i^{i,j}$ exists in the CV at this time. Water enters the CV at an inlet temperature, $T_{in}^{i,j}$, and a mass flow rate $\dot{m}_{in}^{i,j}$. A mass increment of water adjacent to the ice layer, $\dot{m}_f^{i,j}$, freezes and forms a solid ice layer of thickness $\Delta R_i^{i,j}$ over a time step of Δt. The remaining

water flow, $\dot{m}_{out}^{i,j}$, exits the control volume at an outlet temperature, $T_{out}^{i,j}$. The water inside the CV is assumed to be at a uniform mean temperature during the heat transfer process, $T_m^{i,j}$.

The mass transfer equation for the above process in the CV can be written as:

$$\dot{m}_{in}^{i,j} - \dot{m}_{out}^{i,j} = \dot{m}_f^{i,j} = \rho_s 2\pi R_i^{i,j} \frac{\Delta R_i^{i,j}}{\Delta t} \Delta z \tag{1}$$

As water flows through the CV, it cools due to the convective heat loss, which can be written as:

$$\dot{Q}_{conv} = \dot{Q}_{water,in} - \dot{Q}_{water,out} \tag{2a}$$

Eq. (2a) can be expressed as:

$$\frac{Nu\,k_l}{2R_i^{i,j}} 2\pi R_i^{i,j} \Delta z \left(T_m^{i,j} - T_i\right) = \dot{m}_{in}^{i,j} c_{p,l}\left(T_{in}^{i,j} - T_f\right) - \dot{m}_{out}^{i,j} c_{p,l}\left(T_{out}^{i,j} - T_f\right) \tag{2b}$$

The mass of water freezing, $\dot{m}_f^{i,j}$, releases latent heat ($\dot{Q}_{lat}$) at the freezing temperature, T_f; this newly formed ice must cool down further to the temperature of the pre-existing ice layer, T_i, by releasing sensible energy ($\dot{Q}_{ice,sens}$). Therefore, the total energy released in the formation of the ice layer can be written as:

$$\dot{Q}_{rel} = \dot{Q}_{lat} + \dot{Q}_{ice,sens} = \dot{m}_f^{i,j}\left[L + c_{p,s}\left(T_f - T_i\right)\right] \tag{3}$$

Since $T_{wall,ext} < T_i$, the CV cools via radial conduction through the channel wall:

$$\dot{Q}_{cond} = 2\pi\Delta z \frac{\left(T_i - T_{wall,ext}\right)}{\frac{\ln\left(R_{wall,int}/R_i^{i,j}\right)}{k_s} + \frac{\ln\left(R_{wall,ext}/R_{wall,int}\right)}{k_{bs}}} \tag{4}$$

For energy conservation in the CV, the sum of energy convected from the water (sensible), released by ice formation (latent), and removed from the ice layer that is formed (sensible) must be equal to the energy conducted radially through the channel wall

$$\dot{Q}_{conv} + \dot{Q}_{rel} = \dot{Q}_{cond} \tag{5a}$$

On substituting Eqs. $(2b)$, (3) and (4), Eq. $(5a)$ becomes:

$$\dot{m}_{in}^{i,j} c_{p,l}\left(T_{in}^{i,j} - T_f\right) - \left(\dot{m}_{in}^{i,j} - \dot{m}_f^{i,j}\right) c_{p,l}\left(T_{out}^{i,j} - T_f\right) + \dot{m}_f^{i,j}\left[L + c_{p,s}\left(T_f - T_i\right)\right]$$
$$= -2\pi\Delta z \frac{\left(T_i - T_{wall,ext}\right)}{\frac{\ln\left(R_{wall,int}/R_i^{i,j}\right)}{k_s} + \frac{\ln\left(R_{wall,ext}/R_{wall,int}\right)}{k_{bs}}} \tag{5b}$$

The boundary conditions can be written as:

$$T_{wall,ext} = \text{constant at } r = R_{wall,ext}$$

$$T_{in}^{1,j} = T_0$$

$$\dot{m}_{in}^{1,j} = \dot{m}_0$$

The model is evaluated with an initial radius of the annular ice front:

$$R_i^{i,1} = R_0$$

3.2.2 Model simplification

An order-of-magnitude scaling analysis is performed to simplify the overall energy balance given in Eq. $(5b)$. Values for the variables based on the experimental conditions are substituted into the equation to determine the dominant terms. See Appendix B for details of this scaling analysis.

The scaling analysis identifies that the latent heat, $\dot{Q}_{lat}$, dominates over the convected energy, $\dot{Q}_{conv}$, and the sensible cooling of ice, $\dot{Q}_{ice,sens}$. Therefore, Eq. (5b) can be simplified to:

$$\rho_s 2\pi R_i^{i,j} \frac{\Delta R_i^{i,j}}{\Delta t} \Delta z L \approx -2\pi \Delta z \frac{\left(T_i - T_{wall,ext}\right)}{\frac{\ln\left(R_{wall,int}/R_i^{i,j}\right)}{k_s} + \frac{\ln\left(R_{wall,ext}/R_{wall,int}\right)}{k_{bs}}} \qquad (5c)$$

This implies that the radial conduction through the ice layer and the channel wall is the dominant mode that drives the annular ice growth in small channels at small flow rates.

An expression for the annular ice growth period (t_{ann}) can be obtained by integrating Eq. (5c) with respect to R_i from $R_i = R_{wall,int}$ (at $t = 0$) to $R_i = 0$ (at $t = t_{ann}$). It should be noted that although the model is evaluated from an initial radius $R_i = R_0$ at $t = 0$ for comparison to experiments, the lower limit for integration is set to $R_i = R_{wall,int}$ here to obtain an expression for t_{ann} that captures the annular ice growth starting from the channel inside radius.

$$t_{ann} \approx \frac{\rho_s L}{\left(T_i - T_{wall,ext}\right)} \frac{R_{wall,int}^2}{2} \left(\frac{1}{2k_s} + \frac{\ln\left(R_{wall,ext}/R_{wall,int}\right)}{k_{bs}}\right) \qquad (6)$$

This equation indicates that t_{ann} varies directly with the channel size and inversely with the temperature difference between the ice-water interface and the channel wall (as well thermophysical properties of water and channel material). Therefore, a small channel diameter and a large temperature difference would facilitate a faster closure through annular ice. Myers and Low [39] adopted a different modeling approach where they used lubrication theory to approximate the period of annular ice growth in microchannels and arrived at the same conclusion.

3.2.3 Solution algorithm

The above system of Eqs. (1), (2b), and (5b) is solved for the three unknown variables, $\dot{m}_{in}^{i,j}$, $T_{out}^{i,j}$, and $\Delta R_i^{i,j}$ using a numerical procedure implemented in MATLAB. A Nusselt number was derived via a scaling comparison of the convective heat transfer that would cause a sensible temperature change to the heat conduction across the ice-water interface, $h\left(T_m^{i,j} - T_i\right) = k_l \left(\frac{dT}{dr}\right)_{r=R_i}$, such that $Nu = 2 \left(\frac{dT}{dr}\right)_{r=R_i} \Big/ \left(\frac{T_m^{i,j}-T_i}{R_i}\right)$. Assuming a uniform velocity and temperature profile in a cylindrical channel, $\left(\frac{dT}{dr}\right)_{r=R_i}$ scales as $\left(\frac{T_m^{i,j}-T_i}{R_i}\right)$, and therefore $Nu \approx 2$. On substituting Nu in Eq. (2b), the equations can be solved for all control volumes, at a given time, by marching axially along the channel in the direction of flow. The initial value of $T_{out}^{i,j}$ is unknown; an initial guess value of $T_{out}^{i,j} = T_{in}^{i,j}$ is taken and the equations are solved sequentially for all the unknown variables. The mean temperature, $T_m^{i,j}$, is calculated as the mean of $T_{in}^{i,j}$ and $T_{out}^{i,j}$. The solution is then iterated by replacing the guess value with the solution of $T_{out}^{i,j}$ from the previous iteration until the error between calculated value converges to within a threshold of $10^{-5}°\mathrm{C}$. After all the variables are solved at a given time, the solution then marches in time by updating the position of the ice-water interface within each control volume:

$$R_i^{i,j+1} = R_i^{i,j} - \Delta R_i^{i,j} \Delta t \tag{7}$$

3.3 Comparison with the model

In order to compare the model-predicted annular ice growth and channel closing time against the experiments, the external wall temperature during annular ice formation and the water inlet temperature are input to the model based on the experimental conditions. The mass flow rate at the inlet is taken as a constant at all time steps, at a value before freezing begins in the experiments. Even though the flow rate reduces during freezing in the experiments, this constant input mass flow rate to the model has a negligible effect on the predictions because the convection term is negligible in the energy conservation equation (Appendix B). These boundary conditions are

summarized for all of the test cases in Table 2. The channel is divided into 2000 CVs of equal length, $\Delta z = 10^{-5}$ m, resulting in total length of 0.2 m that is equal to the cooled length of the channel in the test cell. Each time step (Δt) is 10^{-3} s. The interface temperature, T_i, is assumed to be equal to the equilibrium freezing temperature of $T_f = 0$°C.

Table 2. Test cases and their corresponding boundary conditions input to the model.

Case	Water inlet temperature, T_0 (°C)	Wall temperature, $T_{wall,ext}$ (°C)	Inlet mass flow rate, $\dot{m}_0$ ($\times 10^{-6}$ kg/s)
A	8	–2	8.33
B	8	–3.5	16.7
C	8	–7	33.3

Fig. 10 shows a comparison between the predicted and measured values of the annular ice front position (normalized as $R_{open}/R_{wall,int}$) versus time at distance of $z/L = 0.95$ from the channel inlet for each of the test cases. R_{open} is calculated as the average of radii of the upper and the lower annular ice fronts, obtained from the images in the experiment using the refraction correction procedure described in Appendix A.

The initial time $t = 0$ s is set as the instant when $R_{open}/R_{wall,int} = 0.8$, *i.e.*, the annular ice layer thickness $(R_{wall,int} - R_i) = 50$ μm. The experimental values of R_{open} are extracted from the high-speed images at an interval of 0.2 s for each trial. The experimental curves show the average of 8 repeated trials for each of the cases. The error bars represent the standard deviation in data for these repeated trials. The trends of the model predictions and the experimental observations

are in reasonably good agreement with each other; some deviations from the experimental values are expected due to the differences between the experimental conditions and modeling assumptions/inputs. For example, the model assumes a constant temperature difference $\Delta T = (T_i - T_{wall,ext})$, entered as an input; however, in the experiments, $T_{wall,ext}$ reduces slightly (or ΔT increases) when the annular ice is thick and loses sensible heat. The model assumes uniform velocity and temperature across the channel cross-section for a CV, while in the experiments, they have radially varying profiles. Also, the thermal conductivity of borosilicate glass is assumed to be $k_{bs} = 1.08$ W/m-K at 25°C, but would be lower at the temperatures encountered in experiments, thereby resulting in slower annular growth than predicted.

As was described in Section 3.2.2, conduction from the outer wall is the dominant heat transfer mode governing the annular ice growth. The expression for annular ice growth time (Eq. (6)) shows that the temperature difference $\Delta T = (T_i - T_{wall,ext})$ is the key factor driving conduction and the annular growth rate. Therefore, it is expected that the channel would close sooner at higher flow rates for which the channel wall is cooler during freezing. This is evident from the model prediction shown in Fig. 10, which matches the experimental trend of decreasing closure times with decreasing external wall temperatures, from case A to case C. It is important to mention here that the water flow rate has no direct influence on the annular ice growth because the convective terms are negligible compared to the conduction terms (see Appendix B). However, the flow rate does play an indirect role in setting the degree of supercooling before nucleation which ultimately determines $T_{wall,ext}$ and hence the temperature difference ($\Delta T = T_i - T_{wall,ext}$) driving annular ice growth.
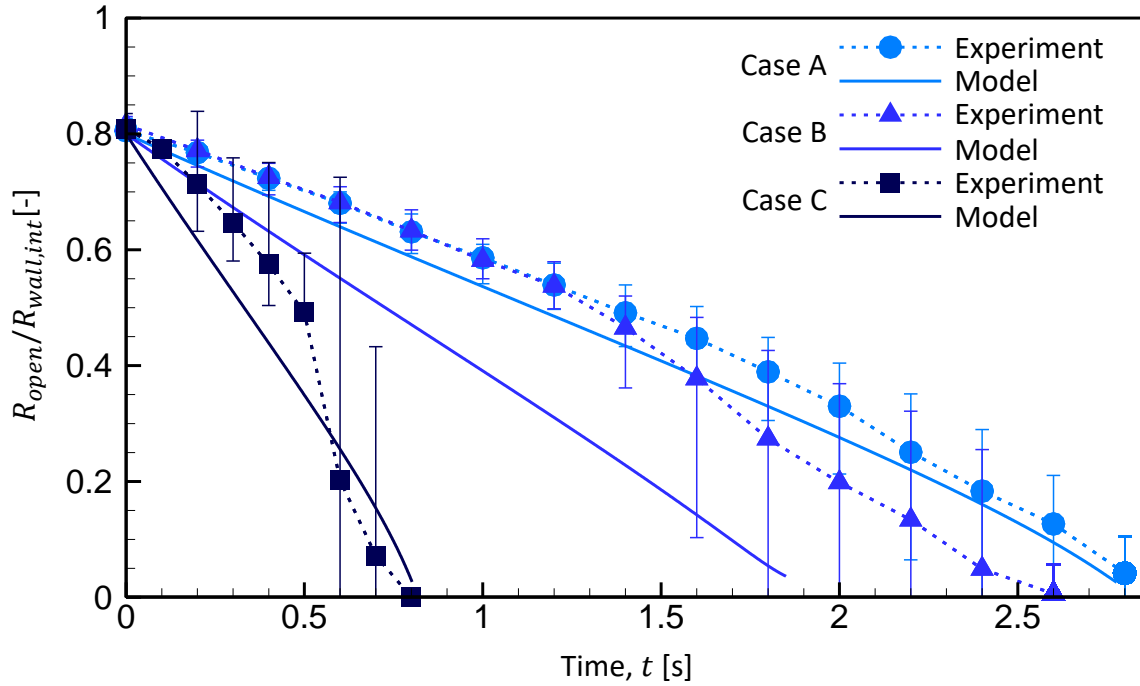
Fig. 10. Comparison of the model-predicted and measured annular growth and closure rates for cases A, B, and C.

4. Conclusions

The freezing of water flowing through a glass channel of small diameter ($D = 500$ μm) is visualized and characterized with a focus on understanding the factors that affect the closing times in small channels, for potential microfluidic ice valve applications. The water is supercooled by exposing the channel external wall to cold N_2 gas, and the freezing process is captured using high-speed imaging until closure occurs in the channel. Freezing is visualized to occur through a mixed mode of ice formation: a thin, sheet-like layer of dendritic ice appears for a brief duration after nucleation, which is followed by slower inward radial growth of a thick, solid ice annulus. The characteristics of each mode are studied using the temperature and flow rate measurements synchronized with the high-speed visualization. Three different water flow rates (0.5, 1, and 2 ml/min) are used to analyze the effect of flow rate on the freezing temperatures and the channel

closing times. A simple finite-volume based model is developed that successfully predicts the annular ice growth duration. The following key conclusions are drawn from the present study:

- Freezing in the channel only starts at a supercooled temperature with the formation of dendritic ice. The latent heat released upon nucleation increases the ice-water interface temperature to the saturation freezing point, T_f, and a constant external channel wall temperature to $T_{wall,ext}$ that depends on the flow rate.

- Following ice nucleation in supercooled water, ice dendrites form a thin layer adjacent to the wall. This layer rapidly propagates along the channel in both streamwise directions from the point of nucleation and covers the entire channel inside surface.

- The dendritic ice formation is followed by the growth of a thick, solid ice annulus which appears at the channel inside circumference along the entire channel length. This ice annulus grows radially inward, at a nearly isothermal wall temperature ($T_{wall,ext,annular}$), and eventually closes the channel.

- The dendritic ice causes some obstruction in the flow path (as indicated by an immediate drop in the water flow rate following dendritic ice appearance) but complete flow blockage and channel closure is ultimately caused by the annular ice for the conditions in this study.

- The annular ice growth is governed by the radial conduction of the released latent heat; convection plays a negligible role, and hence, the flow rate does not have a direct influence on the annular ice growth rate. The flow rate does, however, dictate the degree of supercooling required for nucleation, which determines the temperature difference driving the annular ice growth. In particular, at higher water flow rates, a high degree of supercooling is required to initiate freezing which results in a large temperature difference

and a faster annular ice growth (shorter closing time) compared to lower flow rates. Therefore, the flow rate indirectly affects the channel closing time.

It is also concluded that the latent heat accounts for a large portion of the released energy that needs to be removed to attain channel closure. Therefore, transferring this energy released out of the channel during freezing in the shortest possible time is key to accelerating annular ice growth and increase the closing speed. In practice, the driving temperature difference and the resistance to heat conduction are important parameters that must be considered in the design of high-speed-response ice valves for microfluidic platforms.

Acknowledgement

Appendix A

Supplementary material

Supplementary data associated with the article can be found, in online version, at

Appendix B

B.1.Model scaling analysis

As described in the Section 3.2, a simple control volume-based model is used to predict the

transient location of the annular interface during freezing as well as the total annulus growth

duration in the channel. For the initial time step Δt, the overall energy balance equation for a

single CV of axial length $\Delta z = 10^{-5}$ m is given by Eq. (5b) which can be recast without spatial-

and time-discretization indices as:

$$\dot{m}_{in}c_{p,l}(T_{in} - T_{out}) - \dot{m}_f c_{p,l}(T_{in} - T_{out}) + \dot{m}_f c_{p,l}(T_{in} - T_f) + \dot{m}_f L + \dot{m}_f c_{p,s}(T_f - T_i)$$

$$= -2\pi\Delta z \frac{(T_i - T_{wall,ext})}{\dfrac{\ln(R_{wall,int}/R_i)}{k_s} + \dfrac{\ln(R_{wall,ext}/R_{wall,int})}{k_{bs}}} \tag{8}$$

On the left hand side, the sum of the two terms represents the sensible heat lost by the portion of

water entering the CV that exits without freezing ($\dot{m}_{out}$). The third term represents the sensible

energy lost by the portion of water entering the CV that freezes ($\dot{m}_f$). The fourth term is the latent

heat energy released on freezing. The last term denotes sensible energy lost by solid ice as its

temperature drops from the equilibrium freezing point to the ice-water interface temperature. The

last term has no effect as the ice-water interface is assumed to be at the equilibrium freezing point

$(T_i = T_f)$. The primary variable of interest in Eq. (8) is the growth rate of annular ice $(\Delta R_i / \Delta t)$ which appears implicitly in the rate of ice formation $\dot{m}_f \left(= \rho_s 2\pi R_i \left(\Delta R_i / \Delta t\right) \Delta z\right)$.

An expression for $\Delta R_i / \Delta t$ as shown in Eq. ($5c$) can be deduced by simplifying Eq. (8) based on a comparison of relative orders of magnitude of the above energy terms. The parameters required for estimating the orders of magnitude of these terms are listed in Table B1 for case A.

Table B1. Parameters for case A used to estimate the orders of magnitude of terms appearing in Eq. (8). Parameters denoted by * are estimated based on experimental data.

Parameters	Magnitude
$c_{p,l}$	4187 (J/kg-K)
$c_{p,s}$	1950 (J/kg-K)
L	334000 (J/kg)
ρ_s	916.7 (kg/m³)
Δt	10^{-3} (s)
Δz	10^{-5} (m)
R_0	200 (μm)
$\dfrac{\Delta R_i}{\Delta t}^*$	100 (μm/s)
$R_i^* \left(= R_0 - \left(\dfrac{\Delta R_i}{\Delta t}\right) \Delta t\right)$	199.9 (μm)
$T_i \left(= T_f\right)$	0 (°C)
$\dot{m}_{in}^*$	8.35×10^{-6} (kg/s)
$\dot{m}_f^* \left(= \rho_s 2\pi R_i \dfrac{\Delta R_i}{\Delta t} \Delta z\right)$	1.15×10^{-9} (kg/s)

In addition to the parameters specified in Table B1, the difference between the water inlet and outlet temperatures for the entire channel (with 2000 CVs) is ~6.8°C, as reported in Table 1. and Section 3.2. Accordingly, this temperature difference for a single CV, $(T_{in} - T_{out})$, will at most be of the order 10^{-3} °C, and the temperature difference between the water entering this CV and the freezing temperature $(T_{in} - T_f)$ can at most be of order 10°C. Using these inputs, the orders of magnitude of all energy terms is estimated in Table B2.

Table B2. Estimated orders of magnitude of different energy terms appearing in energy balance Eq. 5b for case A.

Energy terms	Order of magnitude
$\dot{m}_{in} c_{p,l}(T_{in} - T_{out})$	$O(-5)$
$\dot{m}_f c_{p,l}(T_{in} - T_{out})$	$O(-8)$
$\dot{m}_f c_{p,l}(T_{in} - T_f)$	$O(-6)$
$\dot{m}_f L$	$O(-4)$

It is evident from Table B2 that the latent heat energy is one or more orders of magnitude greater than each of the convection energy terms. Neglecting the convection energy terms reduces Eq. (8) to Eq. (5c), which shows a direct balance between the latent heat released with annular ice formation and the radial heat conduction through the annular ice layer and channel wall. In the above discussion, case A is considered as the representative case to demonstrate the order of magnitude of different energy terms but this scaling analysis is also true for cases B and C.

References

[1] S.M. Kim, S.H. Lee, K.Y. Suh, Cell research with physically modified microfluidic channels: A review, Lab on a Chip 8(7) (2008) 1015–1023.

[2] H. Andersson, A. Van den Berg, Microfluidic devices for cellomics: a review, Sensors and Actuators B: Chemical 92(3) (2003) 315–325.

[3] A.J. deMello, Control and detection of chemical reactions in microfluidic systems, Nature 442(7101) (2006) 394–402.

[4] R.C.R. Wootton, A.J. deMello, Microfluidics: analog-to-digital drug screening, Nature 483(7387) (2012) 43–44.

[5] T. Thorsen, S.J. Maerkl, S.R. Quake, Microfluidic large-scale integration, Science 298(5593) (2002) 580–584.

[6] K.W. Oh, C.H. Ahn, A review of microvalves, Journal of Micromechanics and Microengineering 16(5) (2006) R13.

[7] L. Gui, J. Liu, Ice valve for a mini/micro flow channel, Journal of Micromechanics and Microengineering 14(2) (2004) 242.

[8] H. Jerman, Electrically activated normally closed diaphragm valves, Journal of Micromechanics and Microengineering 4(4) (1994) 210.

[9] H. Kahn, M.A. Huff, A.H. Heuer, The TiNi shape-memory alloy and its applications for MEMS, Journal of Micromechanics and Microengineering 8(3) (1998) 213.

[10] D.C. Roberts, H. Li, J.L. Steyn, O. Yaglioglu, S.M. Spearing, M.A. Schmidt, N.W. Hagood, A piezoelectric microvalve for compact high-frequency, high-differential pressure hydraulic micropumping systems, Journal of Microelectromechanical Systems 12(1) (2003) 81–92.

[11] P. Shao, Z. Rummler, W.K. Schomburg, Polymer micro piezo valve with a small dead volume, Journal of Micromechanics and Microengineering 14(2) (2003) 305.

[12] X.Q. Wang, Q. Lin, Y.C. Tai, A parylene micro check valve, IEEE International MEMS 99 Conference, Twelfth IEEE International Conference on Micro Electro Mechanical Systems, Orlando, FL, USA (1999) 177–182.

[13] D.J. Beebe, J.S. Moore, J.M. Bauer, Q. Yu, R.H. Liu, C. Devadoss, B.H. Jo, Functional hydrogel structures for autonomous flow control inside microfluidic channels, Nature 404(6778) (2000) 588–590.

[14] Q. Luo, S. Mutlu, Y.B. Gianchandani, F. Svec, J.M. Fréchet, Monolithic valves for microfluidic chips based on thermoresponsive polymer gels, Electrophoresis 24(21) (2003) 3694–3702.

[15] Y. Liu, C.B. Rauch, R.L. Stevens, R. Lenigk, J. Yang, D.B. Rhine, P. Grodzinski, DNA amplification and hybridization assays in integrated plastic monolithic devices, Analytical Chemistry 74(13) (2002) 3063–3070.

[16] R.H. Liu, J. Bonanno, J. Yang, R. Lenigk, P. Grodzinski, Single-use, thermally actuated paraffin valves for microfluidic applications, Sensors and Actuators B: Chemical 98(2) (2004) 328–336.

[17] R. Pal, M. Yang, B.N. Johnson, D.T. Burke, M.A. Burns, Phase change microvalve for integrated devices, Analytical Chemistry 76(13) (2004) 3740–3748.

[18] C.D. Bevan, I.M. Mutton, Freeze-thaw flow management: a novel concept for high-performance liquid chromatography, capillary electrophoresis, electrochromatography and associated techniques, Journal of Chromatography A 697(1-2) (1995) 541–548.

[19] L. Gui, B.Y. Yu, C.L. Ren, J.P. Huissoon, Microfluidic phase change valve with a two-level cooling/heating system, Microfluidics and Nanofluidics 10(2) (2011) 435–445.

[20] Y. He, Y.H. Zhang, E.S. Yeung, Capillary-based fully integrated and automated system for nanoliter polymerase chain reaction analysis directly from cheek cells, Journal of Chromatography A 924(1) (2001) 271–284.

[21] Z. Chen, J. Wang, S. Qian, H.H. Bau, Thermally-actuated, phase change flow control for microfluidic systems, Lab on a Chip 5(11) (2005) 1277–1285.

[22] C. Si, S. Hu, X. Cao, W. Wu, High response speed microfluidic ice valves with enhanced thermal conductivity and a movable refrigeration source, Scientific reports (2017) 7.

[23] A.E. Sgro, D.T. Chiu, Droplet freezing, docking, and the exchange of immiscible phase and surfactant around frozen droplets, Lab on a Chip 10 (2010) 1873–1877.

[24] J. Schaible, J. Vollmer, R. Zengerle, H. Sandmaier, T. Strobelt, Electrostatic microvalves in silicon with 2-way-function for industrial applications, Transducers' 01 Eurosensors XV, Springer, Berlin, Heidelberg (2001) 900–903.

[25] P.V. Hobbes, Ice Physics, Oxford University Press, Oxford, New York (2010).

[26] M. Akyurt, G. Zaki, B. Habeebullah, Freezing phenomena in ice–water systems, Energy Conversion and Management 43 (2002) 1773–1789.

[27] M.E. Sahagian, H.D. Goff, Fundamental aspects of the freezing process, Freezing Effects on Food Quality, Marcel Dekker, New York, (1996) 1–50.

[28] N.E. Dorsey, The freezing of supercooled water, Transactions of the American Philosophical Society 38 (1948) 247–328.

[29] R.R. Gilpin, The effects of dendritic ice formation in water pipes, International Journal of Heat and Mass Transfer 20 (1977) 693–699.

[30] R.R. Gilpin, The effect of cooling rate on the formation of dendritic ice in a pipe with no main flow, Journal of Heat Transfer 99 (1977) 419–424.

[31] R.R. Gilpin, A study of factors affecting the ice nucleation temperature in a domestic water supply, Canadian Journal of Chemical Engineering 56 (1978) 466–471.

[32] R.R. Gilpin, Modes of ice formation and flow blockage that occur while filling a cold pipe, Cold Regions Science and Technology 5 (1981) 163–171.

[33] H. Inaba, K. Takeya, S. Nozu, Fundamental study on continuous ice making using flowing supercooled water, JSME International Journal Series B 37 (1994) 385–393.

[34] S.L. Braga, J.J. Milón, Visualization of dendritic ice growth in supercooled water inside cylindrical capsules, International Journal of Heat and Mass Transfer 55 (2012) 3694–3703.

[35] N. DesRuisseaux, R.D. Zerkle, Freezing of hydraulic systems, Canadian Journal of Chemical Engineering 47 (1969) 233–237.

[36] F.B. Cheung, J.L. Baker, Transient freezing of liquids in tube flow, Nuclear Science and Engineering 60 (1976) 1–9.

[37] R. Conde, M.T. Parra, F. Castro, J.M. Villafruela, M.A. Rodríguez, C. Méndez, Numerical model for two-phase solidification problem in a pipe, Applied Thermal Engineering 24 (2004) 2501–2509.

[38] E.P. Martinez, R.T. Beaubouef, Transient freezing in laminar tube-flow, Canadian Journal of Chemical Engineering 50 (1972) 445–449.

[39] T.G. Myers, J. Low, An approximate mathematical model for solidification of a flowing liquid in a microchannel, Microfluidics and Nanofluidics 11 (2011) 417–428.

[40] F.G. Alabarse, J. Haines, O. Cambon, C. Levelut, D. Bourgogne, A. Haidoux, D. Granier, B. Coasne, Freezing of water confined at the nanoscale. Physical review letters, 109(3) (2012) 035701.

[41] C. Alba-Simionesco, B. Coasne, G. Dosseh, G. Dudziak, K.E. Gubbins, R. Radhakrishnan, M.J.P.C.M. Sliwinska-Bartkowiak, Effects of confinement on freezing and melting. Journal of Physics: Condensed Matter, 18(6) (2006) R15.

[42] A. Schreiber, I. Ketelsen, G.H. Findenegg, Melting and freezing of water in ordered mesoporous silica materials. Physical Chemistry Chemical Physics, 3(7) (2001) 1185-1195.

[43] A. Jain, Y. Huang, J.A. Weibel, S.V. Garimella, Visualization of ice formation modes and flow blockage during freezing of water flowing in a microchannel, ASME 2016 Heat Transfer Summer Conference, Washington, DC, USA (2016) paper HT2016–7243.

[44] T.A. Kingston, J.A. Weibel, S.V. Garimella, An experimental method for controlled generation and characterization of microchannel slug flow boiling, International Journal of Heat and Mass Transfer 106 (2017) 619–628.

[45] C.S. Lindenmeyer, G.T. Orrok, K.A. Jackson, B. Chalmers, Rate of growth of ice crystals in supercooled water, The Journal of Chemical Physics 27(3) (1957) 822–822.

[46] W. Kong, H. Liu, A theory on the icing evolution of supercooled water near solid substrate, International Journal of Heat and Mass Transfer 91 (2015) 1217–1236.

[47] J.G. Vlahakis, A.J. Bardhun, Growth rate of an ice crystal in flowing water and salt solutions, American Institute of Chemical Engineers Journal 20(3) (1974) 581–591.